Ceramics International 45 (2019) 19617–19626

Contents lists available at ScienceDirect

Ceramics International

journal homepage: www.elsevier.com/locate/ceramint

Effect of swelling agent in the synthesis of porous nanocrystalline nickel-zirconia-ceria composite

V.R.S. Cassimiro[a], R.C. Monteiro[a], R. Bacani[a], L.M. Toscani[b], D.G. Lamas[c,d], S.A. Larrondo[b,e], M.C.A. Fantini[a,*]

[a] Departamento de Física Aplicada, Instituto de Física, Universidade de São Paulo, Rua do Matão 1371, Cidade Universitária, 05508-090, São Paulo, Brazil
[b] UNIDEF, MINDEF, CONICET, Departamento de Investigaciones en Sólidos, CITEDEF, J.B. de La Salle 4397, 1603, Villa Martelli, Pcia. de Buenos Aires, Argentina
[c] CONICET / Laboratorio de Cristalografía Aplicada, Escuela de Ciencia y Tecnología, Universidad Nacional de General San Martín. Martín De Irigoyen 3100, Edificio Tornavía, Campus Miguelete, 1650, San Martín, Pcia. de Buenos Aires, Argentina
[d] Departamento de Física de la Materia Condensada, Gerencia de Investigación y Aplicaciones, Centro Atómico Constituyentes, Comisión Nacional de Energía Atómica, Av. General Paz 1499, 1650, San Martín, Pcia de Buenos Aires, Argentina
[e] Instituto de Investigació, n e Ingeniería Ambiental, Universidad Nacional de General San Martín, Campus Miguelete, 25 de Mayo y Francia, 1650, San Martín, Pcia. de Buenos Aires, Argentina

ARTICLE INFO

Keywords:
Zirconia-ceria
Nickel
IT-SOFC
Catalyst
Micro-mesoporous

ABSTRACT

Porous ceria-zirconia ($Zr_{0.1}Ce_{0.9}O_{2-\delta}\delta$ delete) powders were synthesized by a sol-gel route using inorganic chlorides ($ZrCl_4$ and $CeCl_3{\cdot}7H_2O$) as precursors, block copolymer P123 ($PEO_{20}PPO_{70}PEO_{20}$) as the template and tri-isopropyl-benzene (TIPB) as the swelling agent. These porous materials show high surface area and gas permeability, important properties for Intermediate Temperature-Solid Oxide Fuel Cell (IT-SOFC) and catalytic applications. The samples were prepared with different P123:TIPB (w/w) % ratios (1:0, 1:1, 1:2 and 1:4), as a strategy to increase porosity. The samples were calcined at 400 °C in air to remove the template. Post-synthesis nickel impregnation was planned to obtain 3 and 10 (w/w) % of NiO after calcination. The structure and morphology of the samples were determined by X-ray diffraction (XRD), small angle X-ray scattering (SAXS), nitrogen adsorption isotherms (NAI) and transmission and scanning electron microscopies (TEM and SEM). The resulting materials have high specific surface area ($\approx 110\ m^2.\ g^{-1}$) and a wide pore size distribution of mesopores (3–50 nm). They are formed by nanocrystals ($\approx$ 15 nm) of the predominant ($\approx$ 90%) $Fm\bar{3}m$ cubic phase and by the $P4_2/nmc$ tetragonal phase. The micrographs revealed that the nanocrystalline oxides have mesopores with slit shape and a secondary smaller mesoporosity with a narrow size distribution ($\approx$ 4 nm). An increase of micropore volume (sizes $<$ 2 nm) was observed with the presence of the swelling agent in the synthesis process, ideal for gas diffusion in catalysis and IT-SOFC processes. Temperature programmed reduction (TPR) analysis presented low temperature peaks, a marked increase in the total reduction value and H2 uptake of samples with 3 (w/w)% NiO in contrast to the bare supports. There was no significant further increase in the total reduction value when 10 (w/w)% NiO is incorporated. It is noteworthy that comparing the synthesis methods, all samples presented higher reduction values and H_2 uptake.

1. Introduction

Ceria (CeO_2) and zirconia (ZrO_2) based materials are used in various technological applications [1], mainly as catalyst, as in the automotive converter (Three-Way Catalyst) [2] and in the achievement of highly purified hydrogen flows from renewable resources [3], but also as a key component in the anode of Intermediate Temperature Solid Oxide Fuel Cells (IT-SOFCs) [4].

These materials have been obtained by many different methods. $Zr_xCe_{1-x}O_2$ solid solutions attracted special attention, since they showed better thermal stability and higher oxygen storage capacity (OSC) than the undoped cerium oxide [5–8]. Recently, we have reported a new synthesis method to obtain mesoporous zirconia doped ceria (ZDC), containing 90 mol% CeO_2 and 10 mol% ZrO_2 (also known as CZ material). This mixed oxide was impregnated with 60 (w/w)% NiO, leading to a material with remarkable properties for applications

* Corresponding author.
E-mail addresses: cassimiro.vinicius@gmail.com (V.R.S. Cassimiro), rafacmonteiro@yahoo.com.br (R.C. Monteiro), rbacani@usp.br (R. Bacani), ltoscani@citedef.gob.ar (L.M. Toscani), diego.g.lamas@gmail.com (D.G. Lamas), slarrondo@unsam.edu.ar (S.A. Larrondo), mfantini@if.usp.br (M.C.A. Fantini).

https://doi.org/10.1016/j.ceramint.2019.06.209
Received 14 February 2019; Received in revised form 27 May 2019; Accepted 19 June 2019
Available online 22 June 2019

as anode in IT-SOFCs assemblies and as catalysts for methane combustion [9]. An extensive revision of the literature was made in this former publication, stating the adequacy of this synthesis strategy based on the sol-gel method with a template, working as a structure directing agent. The main idea was to increase the specific surface area of the material to allow better gas transport in gas operation devices, while maintaining thermal stability and control of the nanocrystalline structure up to 1000 °C.

The purpose of this work was to incorporate a swelling agent in the synthesis process previously reported [9] in order to improve the morphology of the material, pointing to catalysis applications.

The pores have proper size and shape to encapsulate amounts of 3 (w/w)%NiO and 10 (w/w)%NiO inside the ZDC porous matrix, much smaller mass concentrations than the former analyzed 60 (w/w)%NiO recommended for anodes of IT-SOFC [9]. The main material synthesis and characterization methods, as well as the characterization techniques, were those already reported in Ref. [9]. Therefore, they will not be reported in details.

2. Materials and methods

2.1. Sample preparation

The synthesis procedure used 1.0 g of Pluronic P-123 (BASF), as the template agent, and tri-isopropyl-benzene (TIPB) as the swelling agent. Different weight ratios of these two agents P123:TIPB (weight concentration ratios of 1:0, 1:1, 1:2 and 1:4) were dissolved and stirred in 16.4 mL of 2 mol L^{-1} HCl solution at 23 °C, before the addition of 3.353 g of $CeCl_3{\cdot}7H_2O$ (99.9% Aldrich) and 0.233 g of $ZrCl_4$ (99.9% Aldrich), to obtain the stoichiometry of the $Zr_{0.1}Ce_{0.9}O_2$ mixed oxide. The solution was stirred for 2 h and its pH was adjusted to 3 by adding NH_4OH [9]. The hydrothermal treatment at 80 °C was done in a Teflon® autoclave for 48 h. The final gel was dried at 60 °C, during one day, in air.

The calcination process was performed in a tubular oven, with a temperature heating rate of 1 °C.min^{-1}, with isotherms of 2 h at 200 °C and 4 h at 400 °C, in air. After switching off the oven, the samples were left to cool inside it [9].

Nickel was incorporated as described in Ref. [9]. The concentration of the nickel precursor was adequate to obtain 3 and 10 (w/w)% of NiO after calcination. The impregnated solid was calcined with the same process defined in Ref. [9].

Table 1 summarizes the nomenclature given to the samples.

2.2. ZDC and Ni/ZDC characterization

The Rietveld crystal structure refinement was performed with TOPAS software [10], using diffractograms obtained with Bruker equipment [9]. The peak shape was assumed as Thomson-Cox-Hastings pseudo-Voigt function [11]. The background of each pattern was fitted by a polynomial function (degree 5) and a 1/x function was selected to fit the low angle region affected by the air scattering.

Nitrogen adsorption isotherms (NAI) data were obtained as described in Ref. [9], performing the same type of calculations to obtain the pore size distribution (PSD), pore volume and pore diameter [12], as well as the specific surface area [13].

Scanning electron microscopy (SEM) and Transmission electron microscopy (TEM) images were obtained in the same conditions of reference [9].

The Small Angle X-Ray Scattering (SAXS) measurements were carried out with a Bruker NANOSTAR camera with a Xenocs Genix 3D source of Cu Kα radiation (λ = 1.5418 Å) operating at 50 kV and 0.6 mA, with a multi-filament Bruker Våntec-2000 bi-dimensional detector. The point focus beam was used and the set up was kept in vacuum (~10^{-2} Torr) to avoid parasitic air scattering. The sample to detector distance was 670 mm, with scattering vector q of $0.012\ Å^{-1} < q < 0.35\ Å^{-1}$). The Inverse Fourier Transform (IFT) was obtained with the PCG software [14].

The Temperature Programmed Reduction (TPR) experiments were performed as described in Ref. [9] with a Micromeritics Chemisorb 2720 equipment. TPR runs were carried out from R.T. to 800 °C and changes in the outlet gas thermal conductivity were monitored with a Thermal Conductivity Detector (TCD), previously calibrated to allow for the quantification of sample H_2 uptake.

Table 1
Nomenclature and identification of the synthesized samples.

Sample	P123:TIPB ratio	NiO [(w/w)%]
ZrCe-0	1:0	0
ZrCe-0-3Ni	1:0	3
ZrCe-0-10Ni	1:0	10
ZrCe-1	1:1	0
ZrCe-1-3Ni	1:1	3
ZrCe-1-10Ni	1:1	10
ZrCe-2	1:2	0
ZrCe-4	1:4	0

3. Results

3.1. X-ray diffraction and Rietveld analysis

Fig. 1 depicts the diffractograms and Rietveld refinement results obtained for the bare samples (without nickel), prepared with different P123:TIPB mass ratio. Table 2 presents the crystal structure model and the initial parameters used in the Rietveld refinement [15]. Table 3 presents the Rietveld refinement results, indicating an overall goodness of fit (S) smaller than 2. Also, the quantitative analysis showed that all samples exhibited a high concentration of the cubic phase, with a low content of the tetragonal one (about 5 wt%). Mean crystallite size and specific deformation (%) for the majority phase (cubic) were evaluated by TOPAS® software using the Double-Voigt Approach [16]. The mean size of the crystallites ($\bar{D}$) is around 22–29 nm and the deformation is around 0.5% in all cases. The poor signal/noise ratio obtained for the tetragonal phase did not allow performing the same analysis for the minor phase.

Fig. 2 presents the diffractograms and Rietveld refinement results obtained for samples with and without 10 (w/w)% NiO, prepared with P123:TIPB mass ratio of 1:0. Table 3 presents the results of Rietveld analysis for all samples. The Rietveld analysis of the samples impregnated with Ni gave similar percentages of the cubic and tetragonal zirconia-ceria phases, as expected. The NiO concentration could not be precisely determined, due to the small intensities and broad NiO diffraction peaks. As our impregnation method is the same as our previous results [9], we consider that nominal and real nickel contents are almost equal. The fitting of the NiO diffraction peaks, assuming pseudo-Voigt functions, provided mean crystallite sizes of (6.9 ± 0.4) nm and (6.0 ± 0.6) nm for ZrCe-0-10Ni and ZrCe-1-10Ni, respectively, using TOPAS® software. The same analysis could not be performed for the samples impregnated with 3 (w/w)% NiO, because of their low intensity peaks.

3.2. Nitrogen isotherms and textural properties

Fig. 3 depicts the nitrogen adsorption-desorption isotherms (NAI), while Fig. 4 the PSD results. BET specific surface area and pore sizes corresponding to maxima in the PSD are presented in Table 4. The materials present type IV isotherms, with H_3 type hysteresis loop, corresponding to pores forming large slits; with pore volumes of ~0.33 m^3/g. The material presents a bimodal size distribution in the mesopore region, with a narrow distribution in the 3–5 nm and a wider size distribution in the 20–50 nm regions. An increment in P123:TIPB

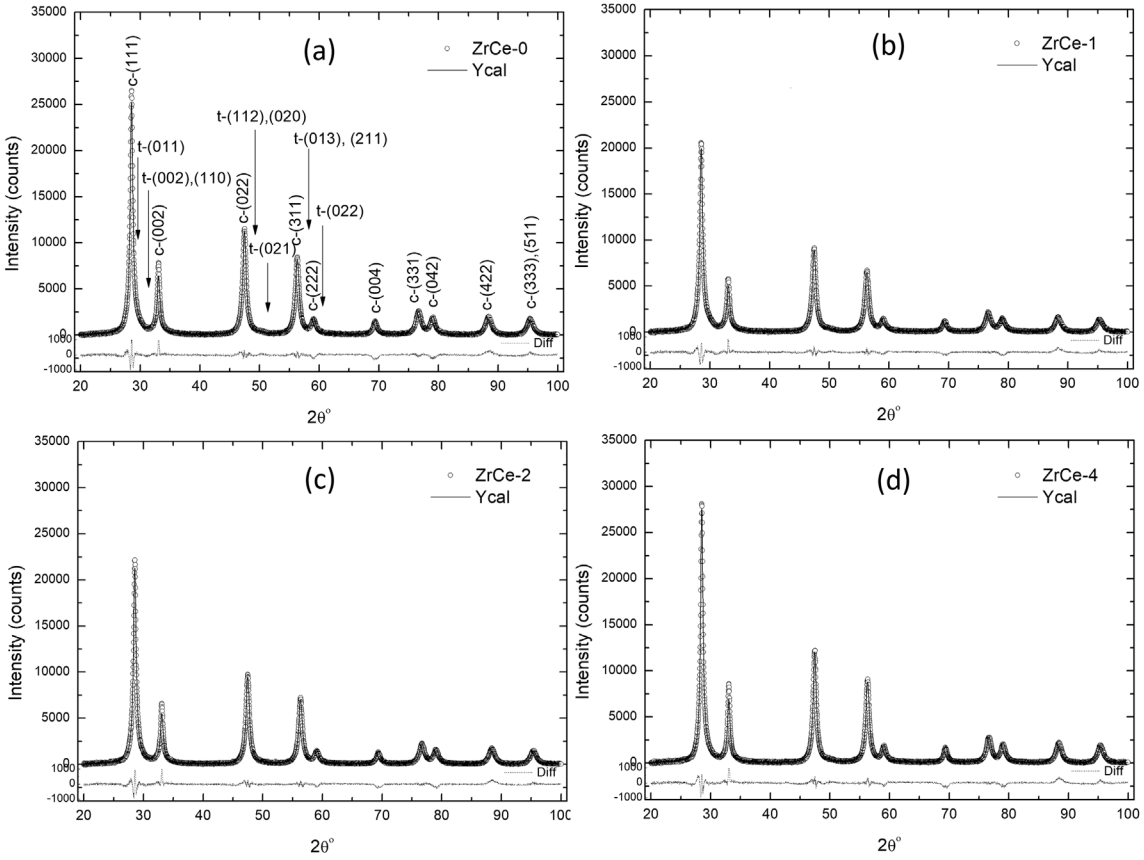

Fig. 1. XRD patterns for samples with experimental data (empty symbols), the Rietveld fitted pattern (line) and the difference plot (dashed line): (a) ZrCe-0 (b) ZrCe- (c) ZrCe-2 and (d) ZrCe-4. The diffraction peaks are indexed in the diffractogram (a).

Table 2
Crystal structure model and initial values used in the Rietveld refinement.
The tetragonal phase data was taken from the ICSD 157620 card [15]

Phase	Group	a = b	c	$\alpha = \beta = \gamma$	Elem.	Wyckoff pos.	x	y	z	Occup.
Cubic $Zr_{0.1}Ce_{0.9}O_{2-\delta}$	$Fm\bar{3}m$ (225)	5.417	5.417	90°	Ce^{4+}	4a	0	0	0	0.01875
					Zr^{4+}	4a	0	0	0	0.00208
					O^{2-}	8c	0.25	0.25	0.25	0.04167
Tetragonal $Zr_{0.1}Ce_{0.9}O_{2-\delta}$	$P4_2/nmc$ (137)	3.599	5.173	90°	Ce^{4+}	2a	0	0	0	0.1125
					Zr^{4+}	2a	0	0	0	0.0125
					O^{2-}	4d	0	0.5	0.216	0.25

Table 3
Rietveld refinement results.

Phase	Parameter	ZrCe-0	ZrCe-1	ZrCe-2	ZrCe-4
Cubic $Zr_{0.1}Ce_{0.9}O_{2-\delta}$	a = b = c [Å]	5.4152 (60)	5.4171 (55)	5.4165 (49)	5.4154 (52)
	Mean crystallite size [Å]	233 (13)	218 (8)	242 (10)	292 (17)
	Weight fraction %	94.4 (1.2)	94.7 (1.8)	94.5 (2.0)	94.3 (2.4)
Tetragonal $Zr_{0.1}Ce_{0.9}O_{2-\delta}$	a = b [Å] c [Å]	3.751 (77) 5.33 (23)	3.709 (65) 5.28 (20)	3.78 (17) 5.34 (49)	3.748 (22) 5.377 (63)
	Weight fraction %	5.6 (1.2)	5.3 (1.8)	5.5 (2.2)	5.7 (2.4)
Refinement quality parameters	R_{exp}	2.27	2.47	2.46	2.28
	R_{wp}	4.41	4.40	4.54	4.52
	R_p	3.27	3.34	3.39	3.31
	R_B (cubic)	1.75	1.534	1.727	1.974
	R_B (tetragonal)	0.347	0.326	0.345	0.414
	S (GoF)	1.94	1.78	1.84	1.98

weight ratio to 1:1 leads to higher BET specific surface area and pore size diameter in the 20–50 nm region. Further increments in swelling agent concentration produce an increment in micropore volume, calculated with t-plot data.

3.3. SAXS results and modelling

The SAXS data of the as-synthesized samples did not present any peaks related to the formation of ordered porous matrices induced by the template together with the swelling agent. The SAXS after

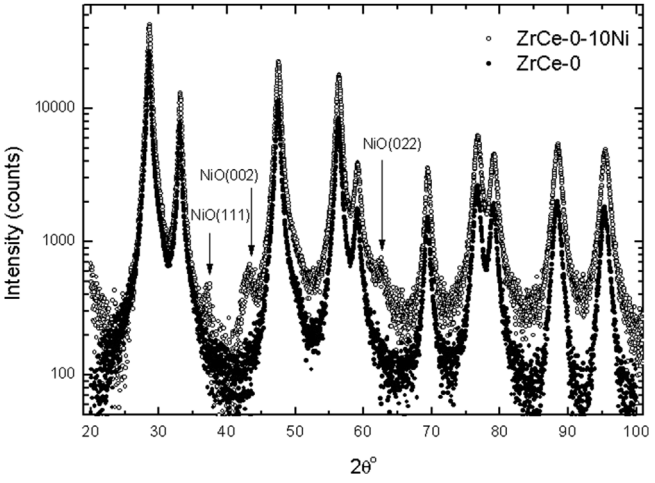

Fig. 2. XRD patterns for samples ZrCe-0 and ZrCe-0-10Ni.

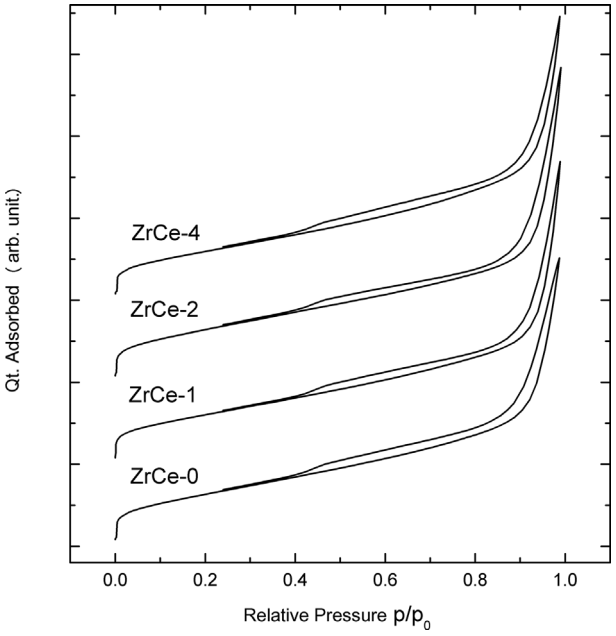

Fig. 3. Nitrogen Adsorption Isotherms of bare ZrCe samples showing the slit like mesoporous type of hysteresis loop.

calcination is presented in Fig. 5. The results show that the TIPB did not alter the porosity significantly. The scattering had risen with the increase in TIPB concentration as an indication of larger porosity, from open and/or closed pores. This tendency can be qualitatively confirmed by the invariant Q, which is the area under the plot I(q). q^2 vs. q. For large q values the scattered intensity follows the Porod's law, showing a decrease with q^{-4}, proving an abrupt electron density variation between the ZDC walls and the pores. The GIFT software [17] was used to evaluate, by the Inverse Fourier Transform (IFT) method the pair distribution function p(r), shown in Fig. 6, for a monodisperse system. For distances larger than 40 nm the *p(r)* values go to zero, in accordance with the large pore values detected by NAI. By considering a polydisperse system of spheres in the GIFT software, the size distribution per number and per volume are depicted in Fig. 7, showing typical sizes of ~4 nm, in accordance with NAI results of the desorption branch. The samples prepared with high TIPB concentrations showed slightly larger pore sizes.

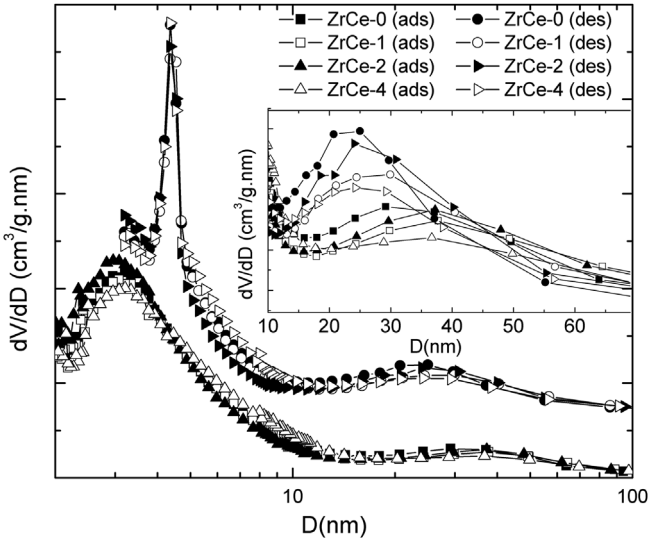

Fig. 4. Pore size distribution with two pore size axis for adsorption and desorption branches.

Table 4
BET specific surface area and pore sizes in maxima of PSD.

Sample	S_{BET} (± 10%) [m^2/g]	V_t[a] [cm^3/g]	V_m[b] [cm^3/g]	Pore size at PSD Maxima in the Adsorption Isotherm branch [nm]		Pore size at PSD Maxima in the Desorption Isotherm branch [nm]	
ZrCe-0	106	0.29	0.014	3.1	31.9	4.4	23.8
ZrCe-0-3Ni	91	0.27	0.004	3.2	30.4	4.5	24.2
ZrCe-0-10Ni	103	0.32	–	3.2	–	–	17.7
ZrCe-1	102	0.30	0.016	3.1	37.7	4.4	28.5
ZrCe-1-3Ni	84	0.29	0.006	3.5	38.6	4.5	29.3
ZrCe-1-10Ni	134	0.46	0.002	3.3	38.7	4.4	29.6
ZrCe-2	118	0.30	0.016	3.0	37.2	4.4	27.5
ZrCe-4	110	0.27	0.023	3.2	34.0	4.4	25.4

[a] Single point total pore volume.
[b] Micropore volume.

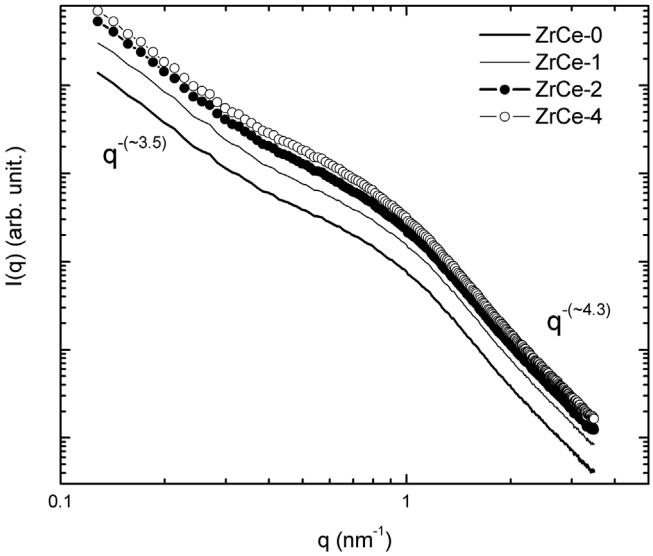

Fig. 5. Small angle X-ray scattering of bare ZrCe samples showing two ranges of scattering angle behavior.

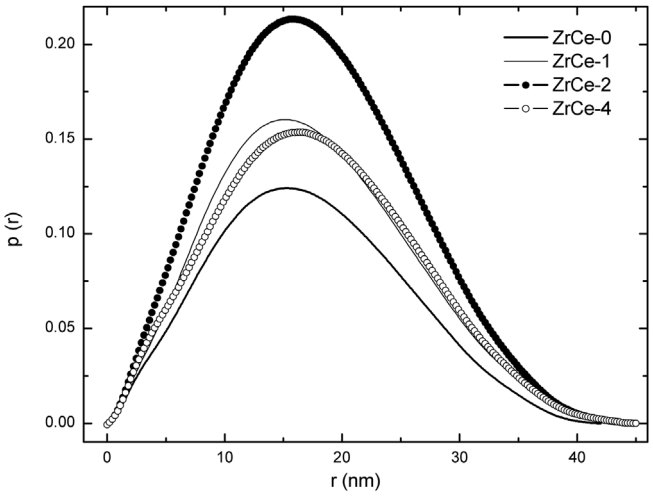

Fig. 6. Pair distribution function obtained from SAXS data assuming a monodisperse system of pores.

3.4. SEM/TEM micrographs

Fig. 8, related to SEM micrographs, confirms the presence of pores in slit form, having sizes of the order of few nanometers, in accordance with the values obtained from NAI and SAXS data. More circular pores were observed as the amount of TIPB in the synthesis increased. This observation is in accordance with the increment observed in micropore volume. TEM images, shown in Fig. 9, also display porosity with an elongated layout and a crystallized material, with domains of the order of few nanometers, in accordance with the crystallite size obtained from XRD measurements.

3.5. TPR analysis

The TPR profiles of the tested samples are plotted in Fig. 10 for the ZrCe-0 and ZrCe-1 samples with different Ni loading. ZrCe-0 sample exhibits a reduction profile with two low-temperature peaks at 415 °C and 525 °C and a high temperature peak at 740 °C. On the other hand, ZrCe-1 sample exhibits two main peaks at 553 °C and 748 °C and a broad shoulder in the low temperature peak. CeO_2-based materials generally exhibit two main peaks: the low temperature peak is usually ascribed to the reduction of Ce surface species and the high temperature peak is usually attributed to bulk Ce reduction [18]. In this case, both samples exhibit these two peaks; however in both cases there is an additional feature at ca. 400 °C. The presence of a small low temperature shoulder in the Zr–Ce-1 sample and a more pronounced feature with a peak maximum at 415 °C in ZrCe-0 sample could reveal the existence of different Ce surface species in each sample that are reduced in subsequent steps. Finally, the reduction profile of ZrCe-0 sample is markedly shifted toward lower temperatures with both the low and high temperature peaks visible at lower temperatures in contrast to ZrCe-1 sample.

Regarding the addition of NiO to ZDC samples, in all cases the samples with 3 (w/w)% NiO and 10 (w/w)% NiO exhibit additional low temperature features which can be ascribed to the reduction of NiO to Ni^0. In the case of ZrCe-0-3Ni and ZrCe-1-3Ni samples, three main peaks are visible with peak maxima at 243 °C, 337 °C and 728 °C for ZrCe-0-3Ni sample and 215 °C, 341 °C and 728 °C for ZrCe-1-3Ni sample. These results indicate that in both samples, the high temperature peak ascribed to the reduction of bulk Ce is slightly shifted to low temperatures compared to the value obtained for the bare support. On the other hand, the peak observed at ca. 340 °C in both samples can be ascribed to concomitant reduction of NiO and surface Ce as no signal is visible at 550 °C, the temperature at which samples without NiO exhibited a strong feature. This implies that the addition of 3 (w/w)% NiO to $Ce_{0,9}Zr_{0,1}O_2$ sample markedly enhances Ce reducibility. It is clear that the main difference in the TPR profiles of ZrCe-0-3Ni and ZrCe-1-3Ni samples is visible in the shape and extent of the low temperature peak visible at ca. 200 °C, since ZrCe-0-3Ni sample exhibits a more intense contribution compared to ZrCe-1-3Ni sample. It should be pointed out that the reduction of NiO generally exhibits two main peaks: the low temperature peak which is usually ascribed to the reduction of NiO surface species and the high temperature peak attributed to both the reduction of bulk NiO species and to species that strongly interact with the support [19–21]. It seems that, in this case, the contribution of surface species to the reduction profile is more significant in the case of

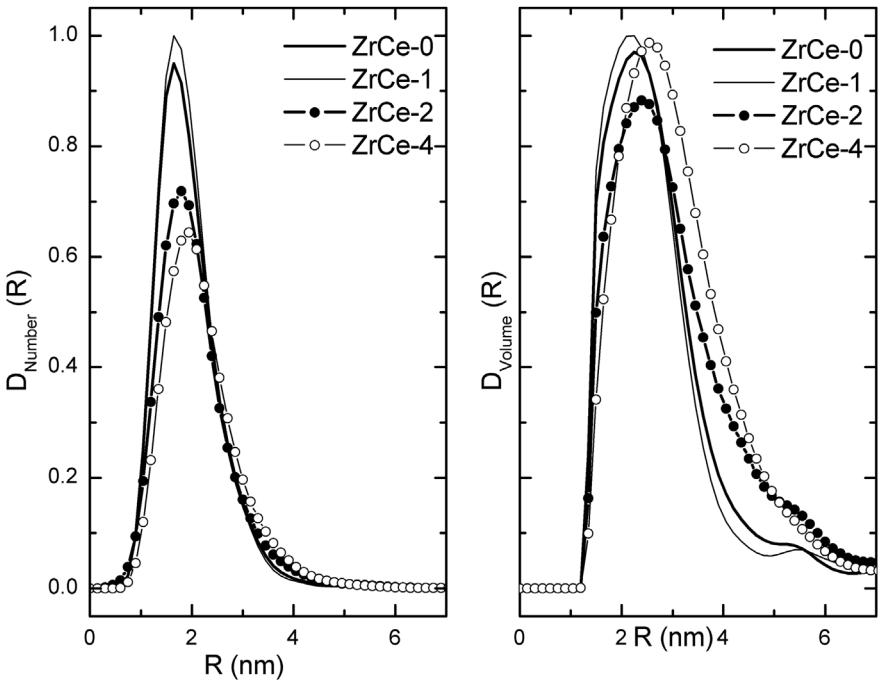

Fig. 7. Number-weighted and volume-weighted size distributions ($D_{Number}(R)$ and D_{Volume} (R), respectively) of scatters from SAXS data.

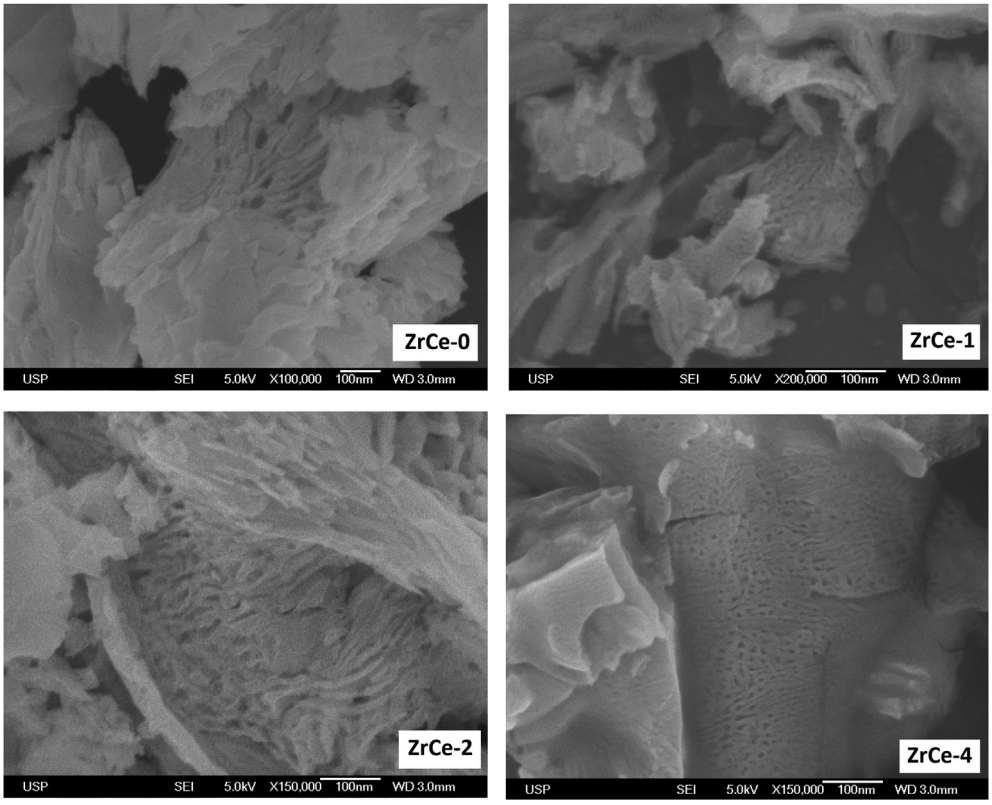

Fig. 8. Scanning electron microscopy (SEM) images of bare samples.

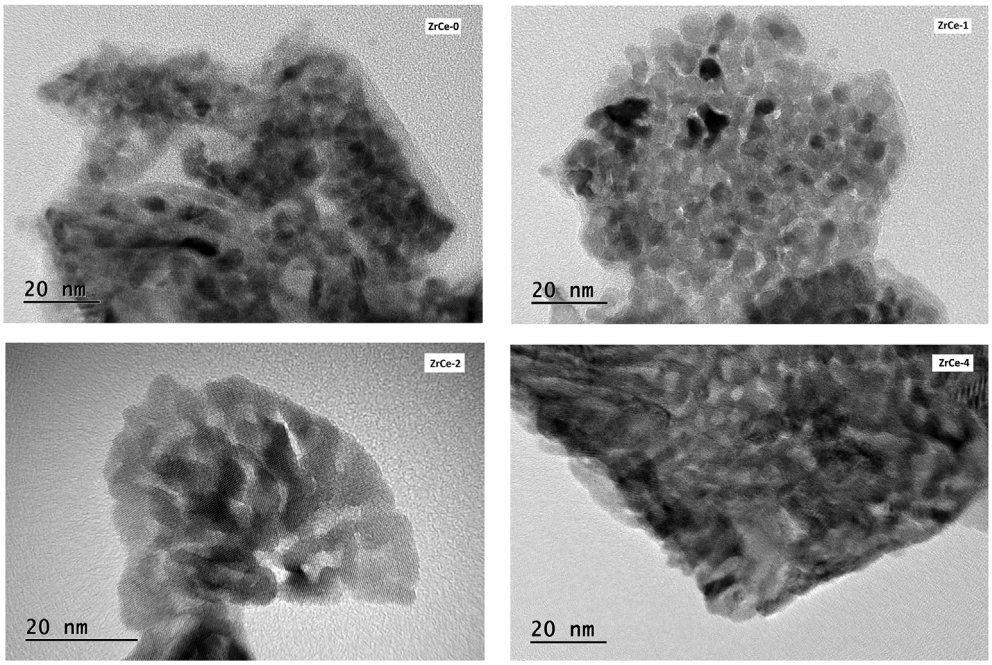

Fig. 9. Transmission electron microscopy (TEM) images of bare samples.

ZrCe-0-3Ni sample.

The addition of 10 (w/w)% NiO to the Ce–Zr support results in TPR profiles with two main contributions in both ZrCe-0-10Ni and ZrCe-1-10Ni samples. The high temperature peak is visible at ca. 730 °C in both cases, virtually at the same temperature as in samples with 3 (w/w)% NiO; however, markedly shifted to low temperatures in contrast to the corresponding bare Ce–Zr supports. This implies that the addition of at least up to 10 (w/w)% NiO promotes the reduction of bulk species. Furthermore, in contrast to samples with 3 (w/w)% NiO, the incorporation of 10 (w/w)% NiO results in the merging of the two low temperature peaks, yielding a large peak at an intermediate temperature of 313 °C and 326 °C for samples ZrCe-0-10Ni and ZrCe-1-10Ni, respectively.

Finally, in Table 5 TPR peak integration results are informed. There is a marked increase in the total reduction value and H_2 uptake of samples with 3 (w/w)% NiO in contrast to the bare supports. However,

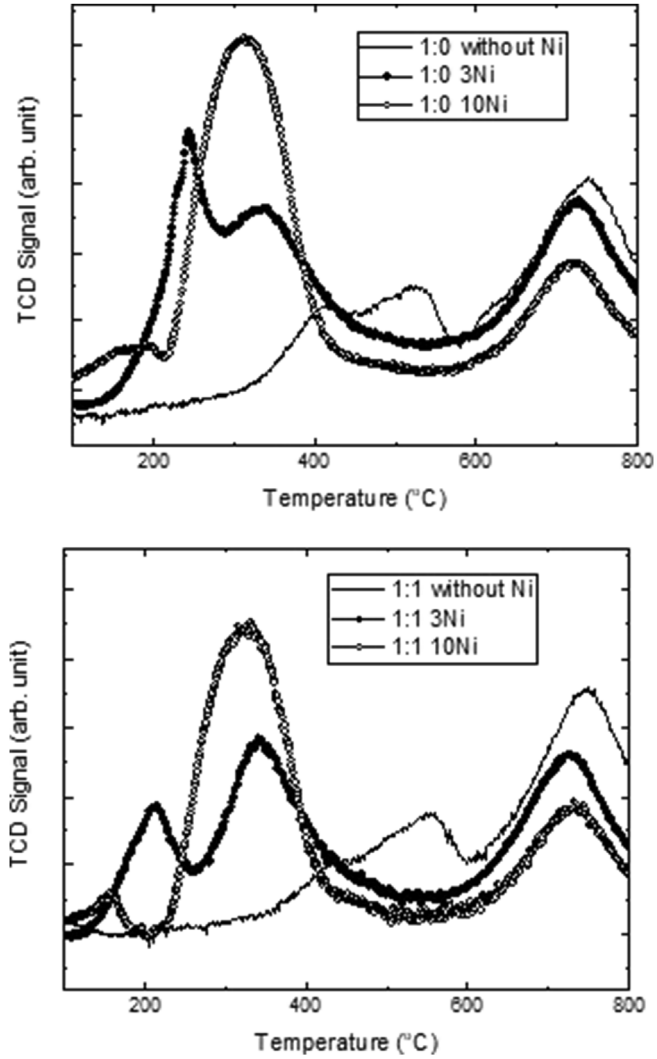

Fig. 10. H_2-TPR profile of the ZrCe-0 and ZrCe-1 bare samples and same samples with Ni.

Table 5
H_2-TPR results.

Sample	Reduction (800 °C) (%)	H_2 uptake (800 °C) (cm^3 (1 atm, 25 °C)/mmolCe^{4+})
ZrCe-0	39.0	4.8
ZrCe-1	31.3	3.8
ZrCe-0-3Ni	52.2	7.4
ZrCe-1-3Ni	43.2	6.1
ZrCe-0-10Ni	49.6	9.4
ZrCe-1-10Ni	43.7	8.3

there is no significant increase in the total reduction value when 10 (w/w)% NiO is incorporated. It is noteworthy that comparing the synthesis methods, all samples prepared with P123:TIPB 1:0 ratio present higher reduction values and H_2 uptake than samples prepared with the 1:1 ratio.

4. Discussion

Previous results on the morphological properties of mesoporous zirconia-based materials are presented in Table 6 [22–31]. The investigation of Ni–CeO_2–ZrO_2 cermets demonstrated excellent resistance toward carbon formation, enhanced reducibility at lower temperatures and stable catalyst activity for more than 200 h [32]. These results motivated researchers to follow new strategies to produce these materials in order to get improved properties, which strongly depend on the composition and synthesis method [33–39]. The preparation method has a huge effect on the physicochemical properties of the resulting materials and, consequently, on their catalytic behavior [39]. In particular, the soft template method allows to produce nanocrystalline phases, whose particle size and morphological properties, such as BET surface area, pore volume and pore diameter strongly influence the catalytic performance [39].

In this work, we introduce a novelty in an already tested sol-gel method with polymeric template previously used to synthesize CeO_2–ZrO_2 mixed oxides: the incorporation of a swelling agent to control the pore size by controlling the size and volume of the micelle. The structure investigated by XRD experiments revealed, for all the samples, the presence of a majority cubic phase $Fm\bar{3}m$ (~95% in weight) and of the tetragonal phase $P4_2/nmc$ in less quantity. The mean crystallite sizes remained from 22 to 29 nm, also in agreement with TEM images, characteristics of a nanocrystalline material, which is reported in many investigations to induce better catalytic performance. The mixture of the two phases can be a disadvantage for anode application in SOFC, especially because they have different thermal expansion coefficients.

The NAI results demonstrated the efficiency of the proposed sol-gel method to produce mesoporous ceria-zirconia powders with high specific surface area (from 110 to 118 $m^2\ g^{-1}$) having slit like pores of significant dimension and volume ($D_{(ads)}$ of 32–37 nm and $Vol_{(ads)}$ of 0.33 $cm^3\ g^{-1}$), compared to previous results (see Table 6). The BJH plots of pore diameters (Fig. 4) presented bimodal distributions for all samples. The first distribution is very narrow and it is localized in the $D_p \approx 3$–5 nm range and the second distribution is wide and spread with $D_p \approx 20$–50 nm. These results indicated the existence of two different pore morphologies. The SEM images clearly showed the slit like mesopores with variable dimensions, but having the same magnitude of the second BJH pore size distribution. The presence of smaller porosity could be observed in the ZrCe-2 sample (Fig. 11), in agreement with the BJH distribution of $D_p \approx 3$–5 nm. The incorporation of TIPB did not result in remarkable different specific surface area or mesopore volume, but contributed to an increase in the dimension of the larger slit like pores, between 15 and 20%, for all TIPB concentrations. The relevant increase of micropore volume indicates the development of a suitable synthesis strategy to improve gas diffusion in catalysis and IT-SOFC processes, which has to be tested in future real devices. The results led to the conclusion that the 1:1 mass ratio of P123/TIPB is enough to expand the pores. The slit like pores are clearly visible in the TEM images, but it was not possible to observe significant morphological modifications between the samples prepared with higher TIPB concentration.

The SAXS data confirmed the negligible difference in the morphology of the samples, because the scattering curves are very similar, except for a larger scattering observed by the ZrCe-2 e ZrCe-4 samples in the region of $0.3 < q < 1.0\ nm^{-1}$, indicating the presence of larger pores. The fact that the BJH analysis of these samples did not show those larger pores is because they are probably closed and not accessible to the nitrogen, but they are detected by SAXS. The scattering curves present three distinct regions. In two regions the Porod's law is verified at low q ($0.15 < q < 0.3\ nm^{-1}$) and at high q ($1 < q < 3.5\ nm^{-1}$), since the scattered intensity decays with q^{-4}. This behavior is observed in two phase systems with two interfaces of different dimensions, like granular porous systems. The Porod regime at low q corresponds to the grain's envelope and at high q to the pores [40]. Considering the analysis by the IFT method, the obtained (r) of monodisperse and diluted scatters, provided a maximum value of 40 nm, being consistent with the NAI results, but this model does not correspond to the pore morphology determined by SEM and NAI. On the other hand, the polydisperse porous system is in accordance with

Table 6
Results reported in the literature about ZrCe samples obtained by a soft template method with copolymers as structure directing agent. For a large list see Ref. [22].

ASMaterial	Copolymer	Pore Structure	Pore size distribution (nm)	Specific surface area ($m^2.g^{-1}$)	Ref.
ZrO_2	P123	*p6mm*	5.8	150	[23,24]
ZrO_2	P123	–	4.2	141–163	[25]
ZrO_2	F127	*p6mm*	4.1	97	[26]
CeO_2	P123	disordered	3.5	86–150	[27,28]
CeO_2	P123	–	10	–	[29]
CeO_2–ZrO_2	P123	disordered	3.3–18.1	32–120	[9,30]
CeO_2–ZrO_2	P123/F127	*p6mm*	3.7–4.1	128–132	[26]
CeO_2–ZrO_2	P123	–	8–12	98–157	[31]
CeO_2–ZrO_2	P123	slit like	3–50 ($3 < D_{max} < 10$)	110–118	this work

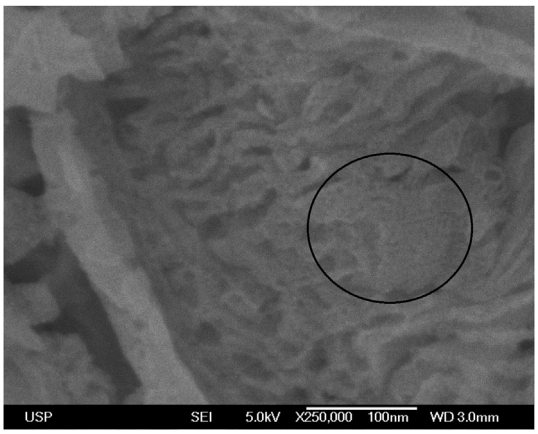

Fig. 11. TEM image of the ZeCe-2 sample with slit like pores and circular pores (circle).

these independent results.

The invariance of the specific surface area with the increase on the TIPB concentration in the synthesis indicates that the morphology is essentially governed by the crystallization process of the mesostructure walls during calcination and less by the skeleton formed by the template through aggregation and later precipitation of metal ions. This behavior is consistent with the observed pore structure reported by Bacani et al. [9,30]. The main effects of the swelling agent in the synthesis process are to induce a wider pore size distribution and an increase in the micropore volume. The other morphological parameters such as the BET surface area and total pore volume did not show remarkable and systematic changes with the introduction of the TIPB in the synthesis. The fact that the increase in the pore diameter occurred for the proportion of P123/TIPB 1:1, but remained unchanged for larger ratios suggests that the extra TIPB is unable to solubilize in the hydrophobic nucleus of the micelles to promote expansion, but contributes to the formation of micropores. A possible mechanism for this synthesis is shown in Fig. 12, where the extra TIPB interacts with the metal ions forming closed pores, not detected by NAI. Even though the hydrophilicities of Si, Ce and Zr precursors are different, this effect was reported by Cao et al. [41], when larger quantities of TIPB did not promote larger pores of SBA-15 samples, because the extra TIPB did not solubilize into the micelles.

H_2-TPR is a very sensitive technique that allows the characterization of samples with reducible species. It is widely used in the characterization of supported and unsupported catalysts. All the H_2-TPR results presented in Table 5 show lower reduction percentage and H_2 uptake values for the ZrCe-1 sample, compared to the ZrCe-0. This result indicates that the TIPB addition to the synthesis process causes no positive effects in the material reducibility. This finding can be attributed to physicochemical changes in the surface of the material, which are not related to morphology, such as chemical bonds and oxygen vacancies,

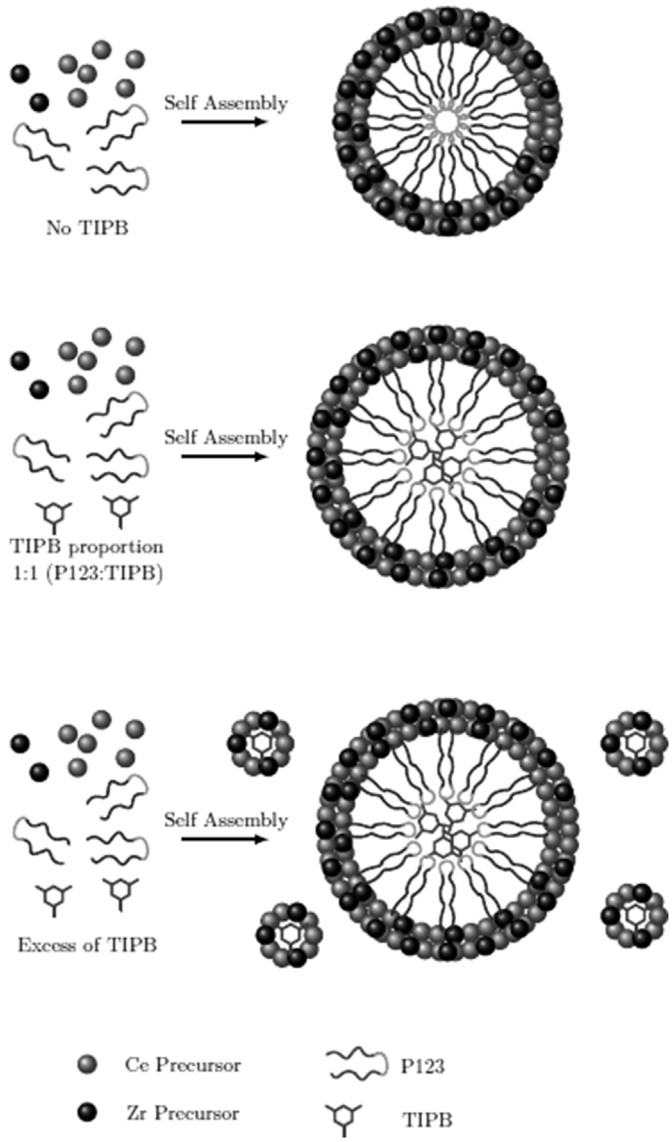

Fig. 12. Pore formation model with different concentrations of swelling agent.

but can be caused by the presence of a hydrophobic agent like TIPB.

Fourier Transform Infra-Red (FTIR) spectrometry studies of the synthesized samples were performed to check possible surface modifications by using TIPB in the synthesis process. FTIR spectra could shine some light on the observed changes of the TPR data, using bands assignments of the literature [42–48]. Indeed, the results (Supplementary Information in Fig. 1S–a and 1S-b) revealed modifications in the transmittance values of the samples synthesized without and with TIPB

(ZrCe-0 and ZrCe-1 samples). There were not observed differences in the wavenumber values of the vibration modes, but the systematic variation of intensities (estimated error < 3%) are evidences of differences on gas absorption properties. A slight and systematic decrease in transmission of the sample synthesized with TIPB was observed in a wide range of wavenumbers. After NiO impregnation with 3 (w/w)% NiO and 10 (w/w)% NiO these modifications were remarkable in the range of 420–580 cm^{-1} and 1050-1800 cm^{-1}. The first range is associated with $ZrCeO_2$ and NiO vibration bands, which have features modified by the presence of TIPB, clearly observed for the sample with high nickel concentration. It is important to point out that smaller amounts of NiO impregnated in the CZ matrix has a greater probability to be located inside the pores, while higher NiO concentrations may close the micropore entrances and cluster on CZ surface, increasing the external surface area, as observed in the NAI results of Table 4. In other words, high NiO concentrations, like 10 (w/w)% NiO, is deleterious for the catalytic properties, in agreement with TPR results. The influence of NiO concentration in the FTIR spectra is more evident in the second range, where the bands associated with water, OH^- and CH vibrations are located. In the range of 1250–1570 cm^{-1} it is possible to observe a decrease in transmittance with the increase of NiO content as well as changes among samples synthesized without and with TIPB. Inversion of transmittance intensities in the range of 1050–1250 cm^{-1} can be observed in the spectra of the samples with 10 (w/w)% NiO made without and with TIPB. This is not the case of the samples with 3 (w/w)% NiO, which showed the same intensity trends in the whole range of wavenumbers. These results clearly indicated that there are alterations in the surface of the CZ material when produced with TIPB that influenced the NiO impregnation process. Of course there are also morphological and NiO concentration effects, like surface and bulk contributions, convoluted in the FTIR results that could not be isolated.

Returning to TPR results, also the slightly higher BET surface area of ZrCe-0-3Ni (91 m^2/g) vs ZrCe-1-3Ni (84 m^2/g), could explain the higher reducibility and shift to lower temperature observed by the former sample. Another property that could affect the TPR results is the mean crystallite size. However, it is probably not the case once it is expected similar values for the 3 (w/w)% NiO materials (ZrCe-0-3Ni and ZrCe-1-3Ni), as it was calculated for the 10 (w/w)% NiO samples. TPR results show clearly that the addition of 3 (w/w)% NiO is enough to promote the reduction of nickel and cerium atoms, suggesting that the surface coverage has to be tailored to allow an adequate catalytic environment for both atoms. The influence of Ni in the reduction of Ce is clear, lowering its working temperature.

5. Conclusions

Summarizing, the synthesis of ceria-zirconia $Zr_{0.1}Ce_{0.9}O_{2-\delta}$ by a template method with a swelling agent produced nanocrystalline powders with predominant cubic phase and a minor content of the tetragonal one. These materials presented high specific surface area with higher pore concentration and expanded pores, the required properties for applications in catalysis and SOFC anodes. The ideal weight ratio of P123/TIPB equal to 1:1 was determined, since higher concentrations of TIPB did not improve significantly some of the above mentioned morphological parameters. The swelling agent does not have a significant influence on the total pore volume. On the other hand, it influences the pore size distribution and micropore volume as well it seems to interfere on the physicochemical properties of the surface. The incorporation of 3 (w/w) % of NiO is sufficient to produce an optimized reduction process of cerium and nickel ions. Higher reduction values and H_2 uptake were observed in processes that occurred at low temperatures (200 °C < T < 800 °C).

Acknowledgements

We acknowledge CNPq and FAPESP for the financial support providing equipment acquisition and fellowships. M.C.A. Fantini is a CNPq researcher.

Appendix A. Supplementary data

Supplementary data to this article can be found online at https://doi.org/10.1016/j.ceramint.2019.06.209.

References

[1] S. Hui, J. Roller, S. Yick, X. Zhang, C. Decès-Petit, Y. Xie, R. Maric, D. Ghosh, A brief review of the ionic conductivity enhancement for selected oxide electrolytes, J. Power Sources 172 (2007) 493–502 https://doi.org/10.1016/j.jpowsour.2007.07.071.

[2] J. Ouyang, Z. Zhao, H. Yang, J. He, S.L. Suib, Surface redox characters and synergetic catalytic properties of macroporous ceria-zirconia solid solutions, J. Hazard Mater. 366 (2019) 54–64 https://doi.org/10.1016/j.jhazmat.2018.11.083"https://doi.org/10.1016/j.jhazmat.2018.11.083.

[3] L.M. Toscani, M.G. Zimicz, T.S. Martins, D.G. Lamas, S.A. Larrondo, In situ X-ray absorption spectroscopy study of CuO–NiO/CeO2–ZrO2 oxides: redox characterization and its effect in catalytic performance for partial oxidation of methane, RSC Adv. 8 (2018) 12190–12203 https://doi.org/10.1039/c8ra01528g.

[4] M. Kuhn, T.W. Napporn, Single-chamber solid oxide Fuel Cell technology—from its origins to today's state of the art, Energies 3 (2010) 57–134 https://doi.org/10.3390/en3010057.

[5] D. Gu, F. Schüth, Synthesis of non-siliceous mesoporous oxides, Chem. Soc. Rev. 43 (2014) 313–344 https://doi.org/10.1039/c3cs60155b.

[6] S. Bernal, G. Blanco, J.J. Calvino, J.C. Hernández, J.A. Pérez-Omil, J.M. Pintado, M.P. Yeste, Some recent results on the correlation of nano-structural and redox properties in ceria-zirconia mixed oxides, J. Alloy. Comp. 451 (2008) 521–525 https://doi.org/10.1016/j.jallcom.2007.04.201.

[7] Q. Yuan, L.L. Li, S.L. Lu, H.H. Duan, Z.X. Li, Y.X. Zhu, C.H. Yan, Facile synthesis of Zr-based functional materials with highly ordered mesoporous structures, J. Phys. Chem. C 113 (2009) 4117–4124 https://doi.org/10.1021/jp806467c.

[8] G. Nahar, V. Dupont, Hydrogen production from simple alkanes and oxygenated hydrocarbons over ceria–zirconia supported catalysts: Review, Renew. Sustain. Energy Rev. 32 (2014) 777–796 https://doi.org/10.1016/j.rser.2013.12.040.

[9] R. Bacani, L.M. Toscani, T.S. Martins, M.C.A. Fantini, D.G. Lamas, S.A. Larrondo, Synthesis and characterization of mesoporous NiO/ZrO_2-CeO_2 catalysts for total methane conversion, Ceram. Int. 43 (2017) 7851–7860 https://doi.org/10.1016/j.ceramint.2017.03.101.

[10] A.A. Coelho, J. Evans, I. Evans, A. Kern, S. Parsons, The TOPAS symbolic computation system, Powder Diffr. 26 (S1) (2011) S22–S25 https://doi.org/10.1154/1.3661087.

[11] D.E. Cox, The Rietveld method. (IUCr monograph on crystallography, No. 5), in: R.A. Young (Ed.), J. Appl. Crystallogr. 27 (1994) 440–441.

[12] E.P. Barrett, L.G. Joyner, P.P. Halenda, The determination of pore volume and area distributions in porous substances. I. Computations from nitrogen isotherms, J. Am. Chem. Soc. 73 (1) (1951) 373–380 https://doi.org/10.1021/ja01145a126.

[13] S. Brunauer, P.H. Emmett, E. Teller, Adsorption of gases in multimolecular layers, J. Am. Chem. Soc. 60 (2) (1938) 309–319 https://doi.org/10.1021/ja01269a023.

[14] O. Glatter, A new method for the evaluation of small-angle scattering data, J. Appl. Crystallogr. 10 (1977) 415–421 https://doi.org/10.1107/S0021889877013879.

[15] D. Lamas, A. Rosso, M.S. Anzorena, A. Fernández, M. Bellino, M. Cabezas, N.W. de Reca, A. Craievich, Crystal structure of pure ZrO_2 nanopowders, Scripta Mater. 55 (6) (2006) 553–556 https://doi.org/10.1016/j.scriptamat.2006.05.035.

[16] D. Balzar, R.L. Snyder, H.J. Bunge, J. Fiala (Eds.), Voigt-function Model in Diffraction Line-Broadening Analysis. -Defect and Microstructure Analysis from Diffraction, International Union of Crystallography, 1999.

[17] O. Glatter, A new method for the evaluation of small-angle scattering data, J. Appl. Crystallogr. 10 (5) (1977) 415–421 https://doi.org/10.1107/S0021889877013879.

[18] P. Fornasiero, G. Balducci, R. Di Monte, J. Kaspar, V. Sergo, G. Gubitosa, A. Ferrero, M. Graziani, Modification of the redox behaviour of CeO_2 induced by structural doping with ZrO_2, J. Catal. 164 (1) (1996) 173–183.

[19] S. Pengpanich, V. Meeyoo, T. Rirksomboon, Methane partial oxidation over Ni/CeO_2-ZrO_2 mixed oxide solid solution catalysts, Catal. Today 93–95 (2004) 95–105 https://doi.org/10.1016/j.cattod.2004.06.079.

[20] H.S. Roh, K.W. Jun, W.S. Dong, J.S. Chang, S.E. Park, Y.I. Joe, Highly active and stable Ni/CeO_2-ZrO_2 catalyst for H_2 production from methane, J. Mol. Catal. 181 (2002) 137–142.

[21] N.W. Hurst, S.J. Gentry, A. Jones, B.D. McNicol, Temperature programmed reduction, Catal. Rev. Sci. Eng. 24 (1982) 233–309 https://doi.org/10.1080/03602458208079654.

[22] D. Gu, F. Schuth, Synthesis of non-siliceous mesoporous oxides, Chem. Soc. Rev. 43 (2014) 313–344 https://doi.org/10.1039/C3CS60155B.

[23] P. Yang, D. Zhao, D.I. Margolese, B.F. Chmelka, G.D. Stucky, Block copolymer templating syntheses of mesoporous metal oxides with large ordering lengths and semicrystalline framework, Chem. Mater. 11 (10) (1999) 2813–2826 https://doi.org/10.1021/cm990185c.

[24] P. Yang, D. Zhao, D.I. Margolese, B.F. Chmelka, G.D. Stucky, Generalized syntheses of large-pore mesoporous metal oxides with semicrystalline frameworks, Nature 396 (6707) (1998) 152–155 https://doi.org/10.1038/24132.

[25] B. Tian, H. Yang, X. Liu, S. Xie, C. Yu, J. Fan, B. Tu, D. Zhao, Fast preparation of

highly ordered nonsiliceous mesoporous materials via mixed inorganic precursors, Chemical Communications (2002) 1824–1825 https://doi.org/10.1039/B205006D.
[26] Q. Yuan, L.-L. Li, S.-L. Lu, H.-H. Duan, Z.-X. Li, Y.-X. Zhu, C.-H. Yan, Facile synthesis of Zr based functional materials with highly ordered mesoporous structures, J. Phys. Chem. C 113 (10) (2009) 4117–4124 https://doi.org/10.1021/jp806467c.
[27] M. Lundberg, B. Skårman, F. Cesar, L.R. Wallenberg, Mesoporous thin films of high surface-area crystalline cerium dioxide, Microporous Mesoporous Mater. 54 (1–2) (2002) 97–103.
[28] M. Lundberg, B. Skårman, L.R. Wallenberg, Crystallography and porosity effects of CO conversion on mesoporous CeO_2, Microporous Mesoporous Mater. 69 (3) (2004) 187–195 https://doi.org/10.1016/j.micromeso.2004.02.009.
[29] C. Ni, X. Li, Z. Chen, H.-Y.H. Li, X. Jia, I. Shah, J.Q. Xiao, Oriented polycrystalline mesoporous CeO_2 with enhanced pore integrity, Microporous Mesoporous Mater. 115 (3) (2008) 247–252 https://doi.org/10.1016/j.micromeso.2008.01.046.
[30] R. Bacani, T.S. Martins, M.C.A. Fantini, D.G. Lamas, Structural studies of mesoporous ZrO_2-CeO_2 and ZrO_2-CeO_2/SiO_2 mixed oxides for catalytical applications, J. Alloy. Comp. 671 (2016) 396–402 https://doi.org/10.1016/j.jallcom.2016.01.213.
[31] X. Li, C. Ni, F. Chen, X. Lu, Z. Chen, "Mesoporous mesocrystal $Ce_{1-x}Zr_xO2$ with enhanced catalytic property for CO conversion", J. Solid State Chem. 182 (2009) 2185–2190 https://doi.org/10.1016/j.jssc.2009.05.001.
[32] P. Kumar, Y. Sun, R.O. Idem, Nickel-based ceria, zirconia, and ceria–zirconia catalytic systems for low-temperature carbon dioxide reforming of methane, Energy Fuels 21 (2007) 3113–3123 https://doi.org/10.1021/ef7002409.
[33] S.S. Kim, S.M. Lee, J.M. Won, H.J. Yang, S.C. Hong, "Effect of Ce/Ti ratio on the catalytic activity and stability of Ni/CeO_2–TiO_2 catalyst for dry reforming of methane, Chem. Eng. J. 280 (2015) 433–440 https://doi.org/10.1016/j.cej.2015.06.027.
[34] F. Sun, C. Yan, Z. Wang, C. Guo, S. Huang, Ni/Ce-Zr-O catalyst for high CO_2 conversion during reverse water gas shift reaction (RWGS)", Int. J. Hydrogen Energy 40 (2015) 15985–15993 https://doi.org/10.1016/j.ijhydene.2015.10.004.
[35] T. Osawa, R. Agata, A. Mouri, Studies of the dissociation activities of methane and carbon dioxide over supported nickel catalyst, J. Mol. Catal. A Chem. 407 (2015) 163–168 https://doi.org/10.1016/j.molcata.2015.06.034.
[36] B. Roy, C.A. Leclerc, Study of preparation method and oxidization/reduction effect on the performance of nickel-cerium oxide catalysts for aqueous-phase reforming of ethanol, J. Power Sources 299 (2015) 114–124 https://doi.org/10.1016/j.jpowsour.2015.08.069.
[37] Z. Qin, J. Ren, M. Miao, Z. Li, J. Lin, K. Xie, The catalytic methanation of coke oven gas over Ni-Ce/Al_2O_3 catalysts prepared by microwave heating: effect of amorphous NiO formation, Appl. Catal. B Environ. 164 (2015) 18–30 https://doi.org/10.1016/j.apcatb.2014.08.047.
[38] M.N. Kaydouh, N. El Hassan, A. Davidson, S. Casaleb, H. El Zakhem, P. Massiani, "Highly active and stable Ni/SBA-15 catalysts prepared by a "two solvents" method for dry reforming of methane, Microporous Mesoporous Mater. 220 (2016) 99–109 https://doi.org/10.1016/j.micromeso.2015.08.034.
[39] D. Devaiah, L.H. Reddy, S.E. Park, B.M. Reddy, "Ceria–zirconia mixed oxides: synthetic methods and applications", Catal. Rev. 60 (2) (2018) 177–277 https://doi.org/10.1080/01614940.2017.1415058.
[40] P. Lindner, T. Zemb, Neutrons, X-Rays and Light: Scattering Methods Applied to Soft Condensed Matter, Elsevier Science B. V., 2002.
[41] L. Cao, T. Man, M. Kruk, Synthesis of ultra-large-pore SBA-15 silica with two dimensional hexagonal structure using triisopropylbenzene as micelle expander, Chem. Mater. 21 (6) (2009) 1144–1153 https://doi.org/10.1021/cm8012733.
[42] P.J. Linstrom, W.G. Mallard (Eds.), NIST Chemistry WebBook, NIST Standard Reference Database Number 69, National Institute of Standards and Technology, Gaithersburg MD, 2001, https://doi.org/10.18434/T4D303.
[43] M. Chelliah, J.B.B. Rayappan, U.M. Krishnan, Synthesis and characterization of cerium oxide nanoparticles by hydroxide mediated approach, J. Appl. Sci. 12 (16) (2012) 1734–1737 https://doi.org/10.3923/jas.2012.1734.1737.
[44] J. Lunacek, O. Zivotský, P. Janos, M. Dosek, A. Chrobak, M. Marysko, J. Bursíe, Y. Jiraskov, Structure and magnetic properties of synthesized fine cerium dioxide nanoparticles, J. Alloy. Comp. 753 (2018) 167–175 https://doi.org/10.1016/j.jallcom.2018.04.115.
[45] M.A. Waghmare, K.S. Pawar, H.M. Pathan, A.U. Ubale, Influence of annealing temperature on the structural and optical properties of nanocrystalline zirconium oxide, Mater. Sci. Semicond. Process. 72 (2017) 122–127 https://doi.org/10.1016/j.mssp.2017.09.036.
[46] V. Biju, M.A. Khadar, Fourier transform infrared spectroscopy study of nanostructured nickel oxide, Spectrochim. Acta, Part A 59 (2003) 121–134 https://doi.org/10.1016/S1386-1425(02)00120-8.
[47] A. Rahdar, M. Aliahmad, Y. Azizi, NiO nanoparticles: synthesis and characterizatio, J. Nanostruct 5 (2015) 145–151 https://doi.org/10.7508/JNS.2015.02.009.
[48] S.V. Ganachari, R. Bhat, R. Deshpande, A. Venkataraman, Synthesis and characterization of nickel oxide nanoparticles by self-propagating low temperature combustion method, Recent Research in Sci, Techn 4 (4) (2012) 50–53.